International Journal of Hydrogen Energy 57 (2024) 918–928

Contents lists available at ScienceDirect

International Journal of Hydrogen Energy

journal homepage: www.elsevier.com/locate/he

Stability and performance of *in-situ* formed phosphosilicate nanoparticles in phosphoric acid-doped polybenzimidazole composite membrane fuel cells at elevated temperatures

Zehua Wang [a,b], Jin Zhang [c], Shanfu Lu [c,**], Yan Xiang [c], Zongping Shao [a], San Ping Jiang [a,b,*]

[a] WA School of Mines: Minerals, Energy & Chemical Engineering, Curtin, University, WA 6102, Australia
[b] National Energy Key Laboratory for New Hydrogen-Ammonia Energy, Technologies, Foshan Xianhu Laboratory, Foshan, 528216, China
[c] Beijing Key Laboratory of Bio-inspired Energy Materials and Devices & School, of Space and Environment, Beihang University, Beijing, 100191, China

ARTICLE INFO

Handling Editor: Fanglin F. Chen

Keywords:
High temperature polymer electrolyte membrane fuel cells
SiO_2/PA/PBI composite membranes
In situ formation of amorphous phosphosilicate
Distribution of relaxation times analysis
Performance

ABSTRACT

One of the effective strategies to pursue the highly durable high-temperature polymer electrolyte membrane fuel cells (HT-PEMFCs) is to introduce inorganic fillers to the phosphoric acid-doped polybenzimidazole (PA/PBI) membranes. Among the inorganic fillers, phosphates such as phosphosilicate are effective in mitigating acid loss at elevated temperatures (200–300 °C). In this paper, the effect of *in situ* formed phosphosilicate on the performance and stability of SiO_2/PA/PBI composite membranes is studied in detail. The mechanical properties and electrochemical performances of the *in situ* formed SiO_2/PA/PBI membranes depend strongly on the content of *in situ* formed $Si_5P_6O_{25}$ fillers and its distribution and microstructure in the membrane. Such *in situ* formed SiO_2/PA/PBI composite membranes show a high conductivity of 53.5 mS cm^{-1} at 220 °C. The assembled single cell shows a maximum peak power density (PPD) of 530.6 mW cm^{-2} and excellent stability at elevated temperature of 220 °C for over 130 h. The exceptional stability at 220 °C is most likely due to the existence of predominant amorphous phosphosilicate phases in the *in situ* formed SiO_2/PA/PBI composite membranes, which inhibits the evaporation and leaching of PA at elevated temperatures. The results indicate the practical application of *in situ* formed SiO_2/PA/PBI composite membranes for HT-PEMFCs.

1. Introduction

The operation of polymer electrolyte membrane fuel cells (PEMFCs) at elevated temperatures or high temperature PEMFCs (HT-PEMFCs) is critical to enhance the tolerance of Pt-based electrocatalysts towards CO and SO_2 pollutants in reformat H_2 fuels and to increase the kinetics for both fuel oxidation reaction and oxygen reduction reactions [1–3]. Among polymer electrolyte membranes for HT-PEMFCs, phosphoric acid-doped polybenzimidazole (PA/PBI) is probably the most successful membrane for application at elevated temperatures [4–6]. PA/PBI membranes can achieve sufficiently high proton conductivity, ranging from 50 to 240 mS cm^{-1} at 160 °C with the acid doping level (ADL) of 6–30 PA molecules per PBI repeat unit [7,8]. There has been significant development in the PA/PBI membrane technologies and the state-of-the-art HT-PEMFC exhibits stable performance for ~18000 h with average voltage loss rates of about 0.7 μV h^{-1} at 160 °C [9,10]. However, PA/PBI membranes still suffer from stability and performance limitations particularly at elevated temperatures due to the inevitable evaporation and dehydration of PA at temperatures greater than 180 °C [11]. Meanwhile, the doped PA molecules are mobile within the PBI matrix, which rearranges from membranes to catalyst layers (CLs) driven by extrusion and electroosmotic drag during the cell operation. The uncontrollable acid distribution and migration would cause PA flooding in anodic CLs, reducing the fuel cell lifetime [11,12]. As shown by Søndergaard and Li et al., the leaching and evaporation of PA dominates the performance deterioration of PA/PBI membranes based HT-PEMFCs, which is accelerated by high current loads, elevated temperatures, and gas flow rates [13]. The acid loss in the membrane will lead to the increase of area-specific resistance and thereby the decrease in the output power density of PEMFCs.

Recent progress in HT-PEMFCs has focused on diverse strategies for increasing the operation temperatures and alleviating the acid leaching

* Corresponding author. WA School of Mines: Minerals, Energy & Chemical Engineering, Curtin University, WA 6102, Australia.
** Corresponding author.
E-mail addresses: lusf@buaa.edu.cn (S. Lu), S.Jiang@curtin.edu.au (S.P. Jiang).

https://doi.org/10.1016/j.ijhydene.2024.01.095
Received 14 November 2023; Received in revised form 3 January 2024; Accepted 8 January 2024
Available online 13 January 2024

at elevated temperatures and high current load, including designing an encapsulating structure in membranes and introducing strong interaction between polymer matrix and PA [14]. For instance, Kannan et al. designed a three-layers PBI membrane, in which the middle acid reservoir layer was coated by two dense PBI layers and reported a superior stability of 10000 h at 180 °C [15]. Quaternary ammonium (QA) groups were introduced into the PBI backbone and successfully reduced the acid leaching due to the strong interaction of basic QA groups and PA molecules [16]. Another approach is to add inorganic fillers such as hydrophilic SiO_2 [17], TiO_2 [18], and TiP_2O_7 [19] into the PBI matrix to form composite membranes. Those inorganic materials contain abundant functional groups on their surface to form hydrogen bonds with PA, thus improving the PA retention ability [17,20]. However, the introduced inorganic fillers would also alter the acid absorption capability and tend to aggregate during the casting process, negatively affecting overall electrochemical performances and mechanical properties of the composite membranes [4]. It has been shown that *in situ* introduced inorganic fillers after membrane casting can increase the dispersion of fillers and enhance the performance [17,21–23]. For example, Chiang et al. reported a one-pot doping method to prepare metal phosphates doped poly(2,5-benzimidazole) composite membranes and showed improved proton conductivity and mechanical property [21]. In recent years, we found that the *in situ* formed phosphosilicate nanoclusters in phosphotungstic acid impregnated mesoporous silica/PBI composite membranes can immobilize PA and significantly reduce the acid leaching, achieving an excellent performance and stability over 2700 h at operating temperature of 200 °C [24]. Further studies showed that operating of phosphosilicate/PA/PBI composite membranes based HT-PEMFCs at elevated temperature of 240 °C substantially increased the stability and CO tolerance in 6.3 % CO-containing H_2 for 100 h under a cell voltage of 0.6 V [25].

The formation process of phosphosilicate by the condensation of silica/alkoxysilane and PA at the temperature range of 150–300 °C is complicated. In early research, Poojary et al. confirmed the existence of $Si_5P_6O_{25}$ crystals with a P/Si ratio of 1.2 [26], while Matsuda et al. reported a SiO_2–P_2O_5 gel using similar synthetic methods, which contains complicated phases of silica, phosphate, water and PA [27]. A high proton conductivity of phosphosilicate was reported as 1.5×10^{-2} S cm^{-1} at 150 °C under 0.4 % RH [28]. Nevertheless, the high proton conductivity of the generated phosphosilicate is related to the enhanced retention of water and PA molecules, which forms Si–*O*–P–OH groups and therefore facilitates the proton transfer [27–29]. Moreover, its proton conductivity decreases at elevated temperatures and prolonged operation due to the formation of $Si_5P_6O_{25}$ crystals and the loss of absorbed PA and water molecule [30]. On the other hand, there are little studies in the intrinsic relationships between stability and performance of SiO_2/PA/PBI composite membrane cells and the variation and properties of *in situ* formed phosphosilicate in the composite membranes.

Herein, we conducted detailed studies on microstructure and properties of phosphosilicate derived from SiO_2 precursors at elevated temperatures, and the impact of *in situ* formed phosphosilicates on mechanical, electrical and electrochemical properties and performances of *in situ* formed SiO_2/PA/PBI-based composite membranes. The best results were obtained on *in situ* formed SiO_2/PA/PBI composite membranes with SiO_2 loading level of 5 wt%, showing the critical role of *in situ* formed phosphosilicate phase in the composite membranes in the microstructure, mechanical properties and performance and stability of SiO_2/PA/PBI composite membranes based HT-PEMFCs at temperatures higher than 200 °C.

2. Experimental

2.1. Materials

SiO_2 nanoparticles (diameter of ~20 nm) were purchased from Macklin reagent, China. Phosphoric acid (PA, 85 %), dimethylacetamide (DMAC), and ethanol were bought from Peking reagent CO., LTD., China. Pt/C (40 wt%) catalyst was supplied from Premetek CO., USA. Pure O-PBI powder was obtained from Shanghai ShengJun CO., China. The gas diffusion layers (GDLs) were purchased from Freudenberg Group, Germany.

2.2. Sample preparation

Phosphosilicate samples were synthesized through the calcination method. Firstly, SiO_2 nanoparticles and PA with a molar ratio of 1/4 were mixed in an agate mortar and then continuously ground to form a white gel. Then, the as-prepared gel was transferred to a lid-covered PTFE beaker and calcined in the furnace in the heating temperature range of 180 and 260 °C for different periods. Samples calcined at 220 °C for 24 and 48 h were denoted as SP-24 and SP-48, respectively. To remove residual PA, the collected gray powder was washed several times with DI water and ethanol until the pH of the solution was close to neutral, followed by drying at 80 °C under vacuum for 12 h.

SiO_2-PA gels were prepared by mixing SiO_2 nanoparticles with PA in different Si/P molar ratios of 1/1.2, 1/2 and 1/4. Meanwhile, $Si_5P_6O_{25}$-PA mixtures were fabricated by mixing the completely washed SP-48 sample with 85 wt% PA solution in the mass ratios of 1/2, 1/1 and 2/1.

Pristine PBI membrane was fabricated by solution casting. Typically, O-PBI powder was first dissolved in DMAC with vigorous stirring, forming a viscous dark-brown liquor. After that, the PBI solution was filtered to remove any impurities, followed by placing it in an ultrasonic cleaner for several hours to remove bubbles. The weight concentration of PBI in DMAC is controlled at around 10 %. Finally, a certain amount of solution taken from the liquor was cast in a glass plate and placed it in a vacuum oven under 60 °C for 24 h to form a pristine PBI membrane.

The preparation of SiO_2/PBI composite membranes was similar to that of pristine PBI membranes. Firstly, SiO_2 nanoparticles were stirred in DMAC solution, following mixed with PBI solution (10 wt% in DMAC). The SiO_2 loading was controlled at 5, 10 and 15 wt% in PBI matrix, denoted as 5%-SP, 10%-SP and 15%-SP, respectively. The thickness of obtained membranes was controlled at around 40 μm. The PA-doped SiO_2/PA/PBI composite and pristine PA/PBI membranes were obtained by immersing the prepared membranes into the 85 wt% PA solution at 80 °C for 3 days.

2.3. Structural characterization

The physical details and microstructure of as-prepared phosphosilicate samples and composite membranes were measured by using powder X-ray diffraction (XRD, D8 Advance diffractometer, Bruker), scanning electron microscopy (SEM, Sigma 300, Zeiss) and the high-resolution transmission electron microscopy (HR-TEM, JEM 2100F, JEOL), respectively. The elemental composition and chemical state of phosphosilicate samples were examined by X-ray photoelectron spectroscopy (XPS, ESCALAB 250Xi, Thermo Fisher Scientific), and its thermal stability in the air was studied through the thermogravimetric analysis (TGA) method. The attenuated total reflection Fourier transform infrared (ATR-FTIR) spectra were obtained in a Nicolet 510 spectrometer.

2.4. Cells assembly and electrochemical measurement

The Pt/C catalyst ink was prepared by mixing the Pt/C catalyst and PTFE solution (20 wt%, DuPont) into the isopropyl alcohol and water solution (v/v = 6/4), followed by dispersing with a high-speed homogenizer. The catalyst ink was dispersed on the surface of the GDLs by ultrasonic spraying method, and the Pt loading was approximately 1.0 mg cm^{-2} for both the cathode and anode. The membrane electrode assemblies (MEAs) were obtained by sandwiching a SiO_2/PA/PBI membrane between two Pt/C coated GDLs with an active area of 4 cm^{-2} without hot-pressing. Then, the MEA_S was assembled in a homemade

fuel cell hardware under the torque of 2.5 Nm. To test the cell, dry H_2 and O_2 with a gas flow rate of 150 mL min^{-1} were fed constantly into the anode and cathode side of the cell.

The electrochemical performances of as-prepared fuel cells were collected through a battery testing system (CT-4008, Neware). The electrochemical impedance spectroscopy (EIS) data of all membranes was measured at a current density of 0.2 mA cm^{-2} between 100 kHz and 0.1 Hz (Parstat 2273, Princeton Applied Research, USA). The through-plane conductivity (σ, S cm^{-1}) of composite membranes was calculated based on the EIS results, in which the first intercept at high frequency (HFR) represents the total ohmic resistance of the fuel cell including the summation of the test configuration resistance (52.1 mΩ cm^2 measured in our previous work [22]). Therefore, the through-plane conductivity was obtained from the following equation:

$$\sigma = \frac{l}{HFR \cdot S - 52.1} \quad (1)$$

where *l* associates the thickness of the membrane, *S* represents the active area of cells and *HFR* is the measured total ohmic resistance in the high frequency.

3. Results and discussion

3.1. Formation and characteristics of phosphosilicate

To understand the *in-situ* formation process of phosphosilicate within the SiO_2/PA/PBI membrane during the cell operation, the interaction between SiO_2 nanoparticles and PA solution was studied at the temperature range of 180–260 °C in the absence of PBI polymer. Fig. 1 exhibits XRD patterns of synthesized SiO_2/PA samples by calcinating at different conditions. Samples calcined at temperatures below 200 °C show a broad peak at around 23° associated with the unreacted amorphous SiO_2 (Fig. 1a), in good agreement with the data reported by Matsuda and Tadanaga et al. on SiO_2–P_2O_5 gel samples [28,30]. As the calcination temperature increased to 220 °C, the XRD patterns shows the well-matched several small peaks with the $Si_5P_6O_{25}$ crystals (JCPDS: 40–0457) [24,30] and the intensities of peaks increased with the increase of the calcination temperature. This indicates that the phosphosilicate phase starts to form at the temperature of 220 °C. At this phase formation temperature, the XRD pattern of the formed phsphosilicates also increases with the heat treatment time (Fig. 1b), suggesting the growth of $Si_5P_6O_{25}$ particles. However, the reduced peak intensity of the mixed SiO_2/PA sample calcined for 48 h, SP-48, may be caused by the

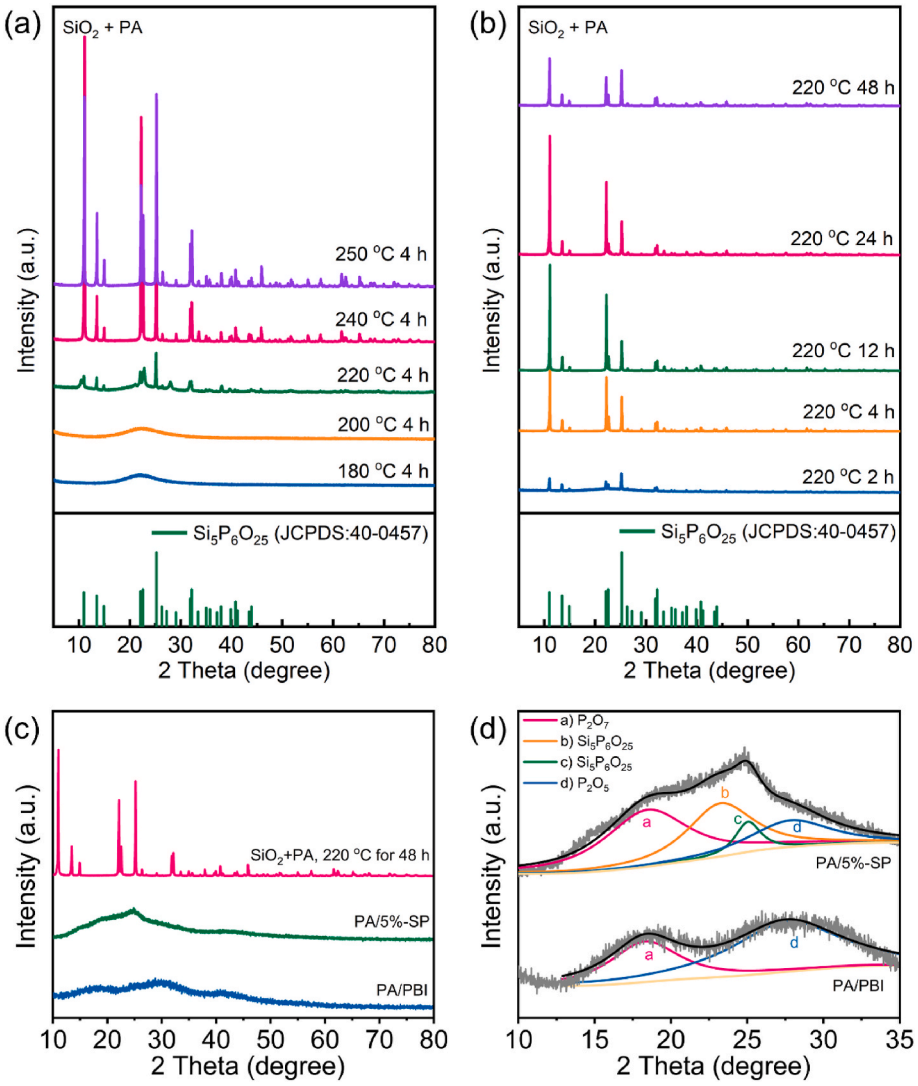

Fig. 1. The XRD patterns of mixed SiO_2+PA samples calcined (a) at the temperatures for 4h and (b) at 220 °C from 2 to 48 h, (c) XRD patterns of SiO_2+PA sample, PA/5%-SP membrane and pristine PA/PBI membrane after the heat treatment at 220 °C for 48 h, and (d) enlarged area of XRD patterns of PA/5%-SP membrane and pristine PA/PBI membrane after the heat treatment at 220 °C for 48 h.

fragmentation of $Si_5P_6O_{25}$ due to the prolonged heat treatment. Crystallographic studies revealed that $Si_5P_6O_{25}$ crystallizes in the trigonal $\bar{R}3$ space group, which contains three inequivalent Si^{4+} sites to form SiO_6 octahedral and SiO_4 tetrahedral simultaneously [31]. Moreover, the PO_4 tetrahedral that shares corners with SiO_6 octahedral and SiO_4 tetrahedral is derived from the coordination of unique P^{5+} and O^{2-} atoms [26,31]. Although the proton conductivity of pure $Si_5P_6O_{25}$ phase is negligible, abundant terminal oxygen in $Si_5P_6O_{25}$ facilitates the formation of Si–*O*–P–OH groups by absorbing water or PA molecules; therefore, leading to a good protonic conductivity at around 160 °C [30,32].

The phase of the pristine PA/PBI and SiO_2/PA/PBI composite membrane with 5 % SiO_2 (PA/5%-SP) after heat-treatment at 220 °C for 48 h was also examined and the results are shown in Fig. 1c and d. Two broad peaks at around 19° and 27° are shown in both pristine and composite membranes (Fig. 1d), which is associated with P_2O_7 and P_2O_5 phases decomposed from PA at elevated temperatures [24]. In the case of PA/5%-SP composite membrane, two broad peaks located at 23° and 25° were detected, well matching with the $Si_5P_6O_{25}$ phase as in the case of SiO_2+PA sample calcined at 220 °C for 48 h (Fig. 1c). In comparison with the sharp and well-defined XRD patterns of $Si_5P_6O_{25}$ phase formed in the mixed SiO_2+PA samples, the significantly depressed and broad characteristic peaks associated with $Si_5P_6O_{25}$ phase indicate that phosphosilicate phases *in situ* formed within SiO_2/PA/PBI composite membranes after heat-treatment at 220 °C are dominantly amorphous with small content of crystalline phase (Fig. 1d), very different from the fully crystalline $Si_5P_6O_{25}$ phase formed in the mixed SiO_2+PA samples heat-treated under identical conditions. The existence of such dominant amorphous $Si_5P_6O_{25}$ phase *in situ* formed within SiO_2/PA/PBI composite membranes is most likely related to the inhibition effect of PBI matrix in the crystallization of $Si_5P_6O_{25}$ phase during the heat-treatment. As will be shown in following sections, the formation of such predominant amorphous phosphosilicate phases plays critical role in the significantly enhanced electrical and electrochemical performance and stability of SiO_2/PA/PBI composite membranes at elevated temperatures.

The morphologies of SiO_2 precursors and as-prepared phosphosilicate samples were observed by SEM and the results are shown in Fig. 2. The average diameter of SiO_2 precursors is typically 20 nm and uniformly distributed (Fig. 2a and **b**). After calcining SiO_2/PA mixture at 220 °C for 4 h, the morphology of the calcined sample remains unchanged, similar to the SiO_2 precursors (Fig. 2c). The relatively weak XRD characteristic peaks associated with $Si_5P_6O_{25}$ (see Fig. 1a) indicates the presence of amorphous SiO_2 nanoparticles with the formation of $Si_5P_6O_{25}$ phase [28]. The contents of nanoparticles decreased significantly when the calcination time was extended to 24 h (SP-24), see the orange circle in Fig. 2d. At the same time, there appear large number of plate-like particles with typical size of about 500 nm to 2 μm. Nanoparticles are generally attached to the edge of large plate-like particles (Fig. 2f). In comparison with that calcined at 220 °C for 48 h, the sample only showed irregular and plate-like particles with no nanoparticles (Fig. 2g). Those results indicate that the SiO_2 nanoparticles gradually transferred into $Si_5P_6O_{25}$ phase with the characteristic plate-like structure under calcination at 220 °C. After calcined at 220 °C for 48 h (SP-48), the as-prepared $Si_5P_6O_{25}$ phase shows a dense and smooth surface, indicating the complete formation of $Si_5P_6O_{25}$, consistent with the XRD data (Fig. 1b). Interestingly, the surface of as-prepared $Si_5P_6O_{25}$ particles contains an amorphous layer with an average thickness of 20 nm (Fig. 2i), similar to the reported pyrophosphate materials that have been considered as the phosphorus-rich layer for proton transfer [33].

Fig. 3 shows the XPS curves of mixed SiO_2/PA samples calcined at 220 °C for 24 and 48 h (SP-24 and SP-48), revealing the composition and valence state of Si, P and O elements on the surface of obtained $Si_5P_6O_{25}$ phase. The high-resolution spectra of Si 2p in the SP-24 and SP-48 samples exhibited a single peak closely located at 130 eV and 130.4 eV, respectively, which can be further divided into two peaks of Si $2p_{1/2}$ and $2p_{3/2}$ by the Gaussian fitting method [29]. Note that the 2p peak of the Si–O bond in the SP-24 sample shifted to a lower binding energy,

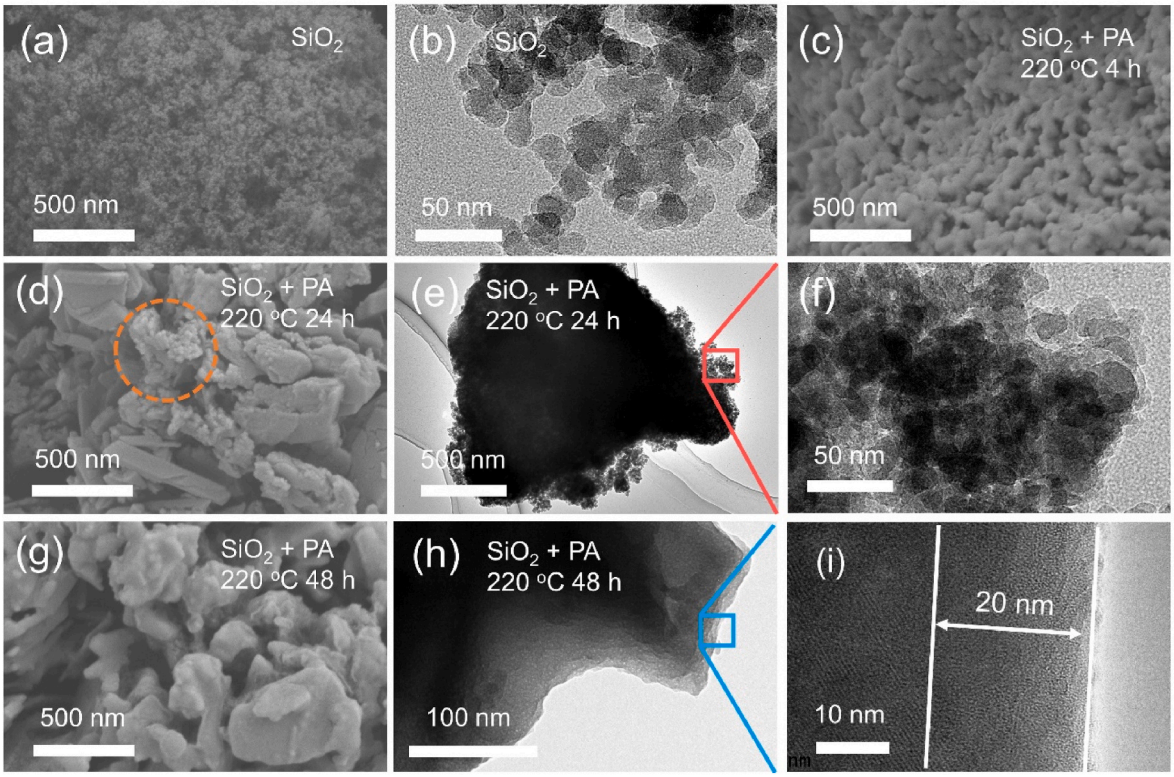

Fig. 2. The morphologies of SiO_2 precursors measured by (a) SEM and (b) TEM, (c) SEM image of mixed SiO_2/PA sample heat-treated at 220 °C for 4h, SEM and HR-TEM images of mixed SiO_2/PA sample heat-treated at 220 °C for (d–f) 24h and (g–i) 48h. Samples were completely washed with DI water to remove residual acid before the examination.

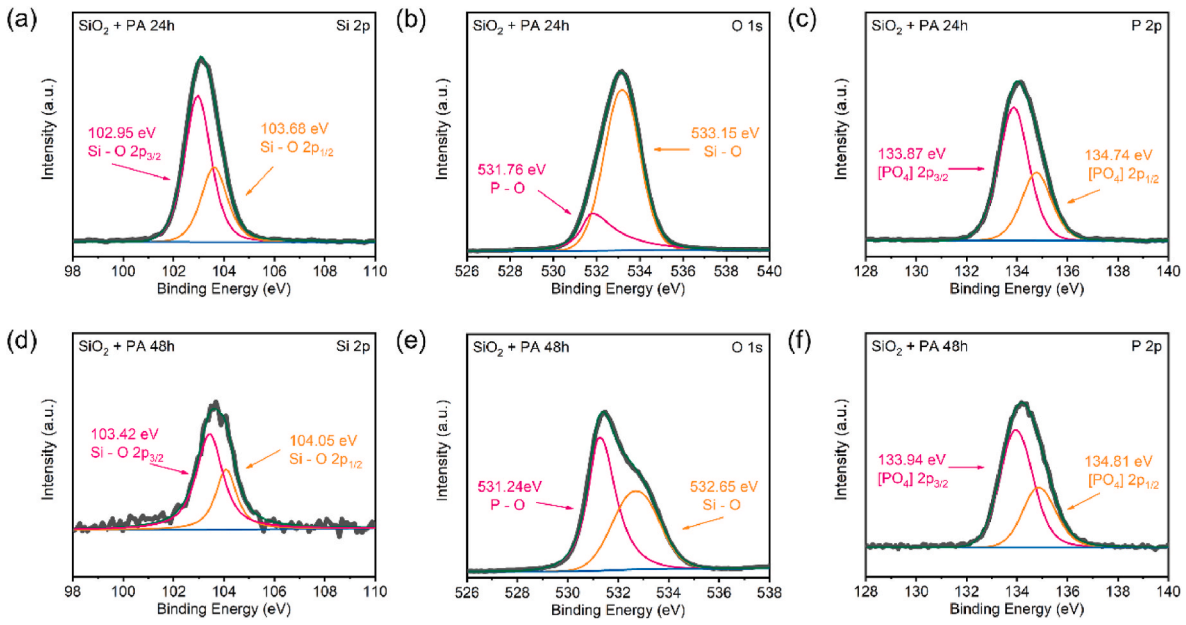

Fig. 3. XPS spectra of Si, O and P elements of mixed SiO_2/PA samples calcined at 220 °C for (a, b and c) 24 h (SP-24) and (d, e and f) 48 h (SP-48).

suggesting the existence of SiO_2 as the SiO_6 octahedral and SiO_4 tetrahedral in $Si_5P_6O_{25}$ process more electrons than SiO_2 [34]. The O 1s spectra of the samples can be deconvoluted into two distinct peaks centered at about 531 and 533 eV, respectively (Fig. 3b and **e**). A small peak at 531.76 eV in SP-24 can be ascribed to the P–O bond while the sharp peak at 533.15 eV is associated with the Si–O bond [29,34]. In comparison, the peak of the P–O bond located at 531.24 eV in SP-48 sample occupied a dominant position than that of the Si–O bond at 532.65 eV, confirming that nanoparticles on the surface of SP-24 sample are unreacted amorphous SiO_2. Additionally, the P 2p spectra shown in Fig. 3c and **f** exhibit a sharp peak at approximately 134 eV for both SP-24 and SP-48 samples, which is consistent with the P–O bond of PO_4 tetrahedral.

Fig. 4 shows the phase change and characteristics of SiO_2/PA sample after calcined at 220 °C for 48 h (SP-48) before and after the washing procedure. It is clear that the characteristic peaks of the $Si_5P_6O_{25}$ phase became sharper after washing owing to the removal of residual PA on the surface of the $Si_5P_6O_{25}$ (Fig. 4a). After the complete removal of PA, the sample represents the pristine $Si_5P_6O_{25}$ phase, as shown by the substantially increased peak intensities. This is also confirmed by the TGA data (Fig. 4b). The first weight loss (25–200 °C) for the samples before and after the washing is assigned to be the desorption of bounded water molecules. In comparison, the as-washed SP-48 sample shows a stable platform in the temperature range of 200–800 °C, while the as-

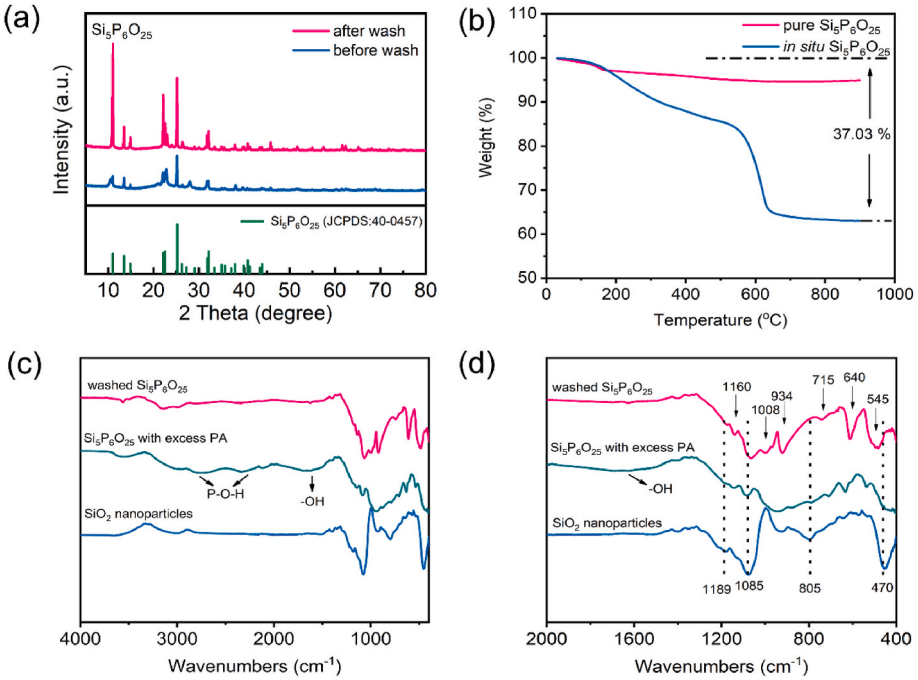

Fig. 4. (a) XRD patterns, (b) TGA curves and (c and d) The FT-IR spectra of SiO_2/PA sample after calcined at 220 °C for 48 h (SP-48) before and after washing treatment. The FT-IR spectrum of SiO_2 nanoparticles is also displayed in c and d.

prepared sample exhibited a slow weight loss when the temperature increased to about 500 °C, indicating that bounded PA on $Si_5P_6O_{25}$ surface is stable [35]. Nevertheless, further increasing the temperature to about 650 °C would cause rapid weight loss, which can be assigned to the evaporation of PA at elevated temperatures [35,36]. In the FT-IR spectrum of as-prepared SP-48 sample before washing, several peaks at 1160 and 1008 cm^{-1} can be assigned to the existence of Si–*O*–P bond in $Si_5P_6O_{25}$, while small peaks at 545, 640 and 715 cm^{-1} are derived from the crystallization of $Si_5P_6O_{25}$ [34] (Fig. 4c and **d**). Evidence peaks at approximately 934 cm^{-1} and 3400 cm^{-1} can be found, related to the stretching mode of surface –OH groups [34,37]. Besides this, the broad peak at around 2500 cm^{-1} suggests the existence of rich phosphate groups terminated with a hydroxyl group on the surface of $Si_5P_6O_{25}$ [34,37].

3.2. Characteristics of the in-situ formed SiO_2/PA/PBI composite membranes

As the dispersion of inorganic fillers in PBI membranes is critical to the mechanical properties and electrochemical performances, microstructures of SiO_2/PBI composite membranes were studied in detail. Fig. 5 shows the cross-section SEM images of pristine PBI and SiO_2/PBI composite membranes. Pristine PBI membrane exhibits a smooth and dense structure (Fig. 5a), while the microstructure of composite membranes depends strongly on the content of SiO_2 fillers. Homogeneous morphology without isolated pores was observed when the SiO_2 loading level was 10 wt% (10%-SP, see Fig. 5b and **c**), confirming good compatibility of SiO_2 fillers with the PBI matrix. Fig. 5f–h exhibits the elemental mapping images of carbon, oxygen and silicon in the 10%-SP composite membrane, which also indicates a uniform distribution of SiO_2 in the PBI matrix. However, aggregated particles were observed in the composite membrane when the SiO_2 loading reached 15 wt% (Fig. 5d), generating cracks and voids within the composite membrane. Although more SiO_2 loading positively affects the proton conductivity and PA retention of SiO_2/PA/PBI composite membranes, the resulting defects would damage their mechanical properties [17]. Since the PA amount significantly influences the proton conductivity of PBI-based membranes, we also compared the acid doping level (ADL) of pristine PBI, 5%-SP and 10%-SP membranes, exhibiting slightly increased PA absorption ability of around 6.8, 6.9 and 7.1 PA molecules per PBI repeat unit, respectively. Certainly, the facilitated acid adsorption ability of composite membranes is attributed to the hygroscopicity of SiO_2.

The hydrogen penetration through the membrane is one of key factors affect the cell durability, which is related to structural defects in the composite membranes derived from the aggregation of inorganic fillers [38]. The surface and cross-section SEM images of heat-treated 5%-SP and 10%-SP composite membranes are displayed in Fig. 5i–l. The surface of 5%-SP was smooth and homogeneous after heat-treatment at 220 °C for 48 h (Fig. 5i). By contrast, the 10%-SP treated under the same condition had a rough surface with cracks and holes (Fig. 5j). The backscattering electron images shown in Fig. 5k and **l** confirmed that *in situ* generated $Si_5P_6O_{25}$ particles concentrated on the surface of 10%-SP, while uniformly distributed in 5%-SP composite membrane. The mechanical properties of the membranes were also measured to further

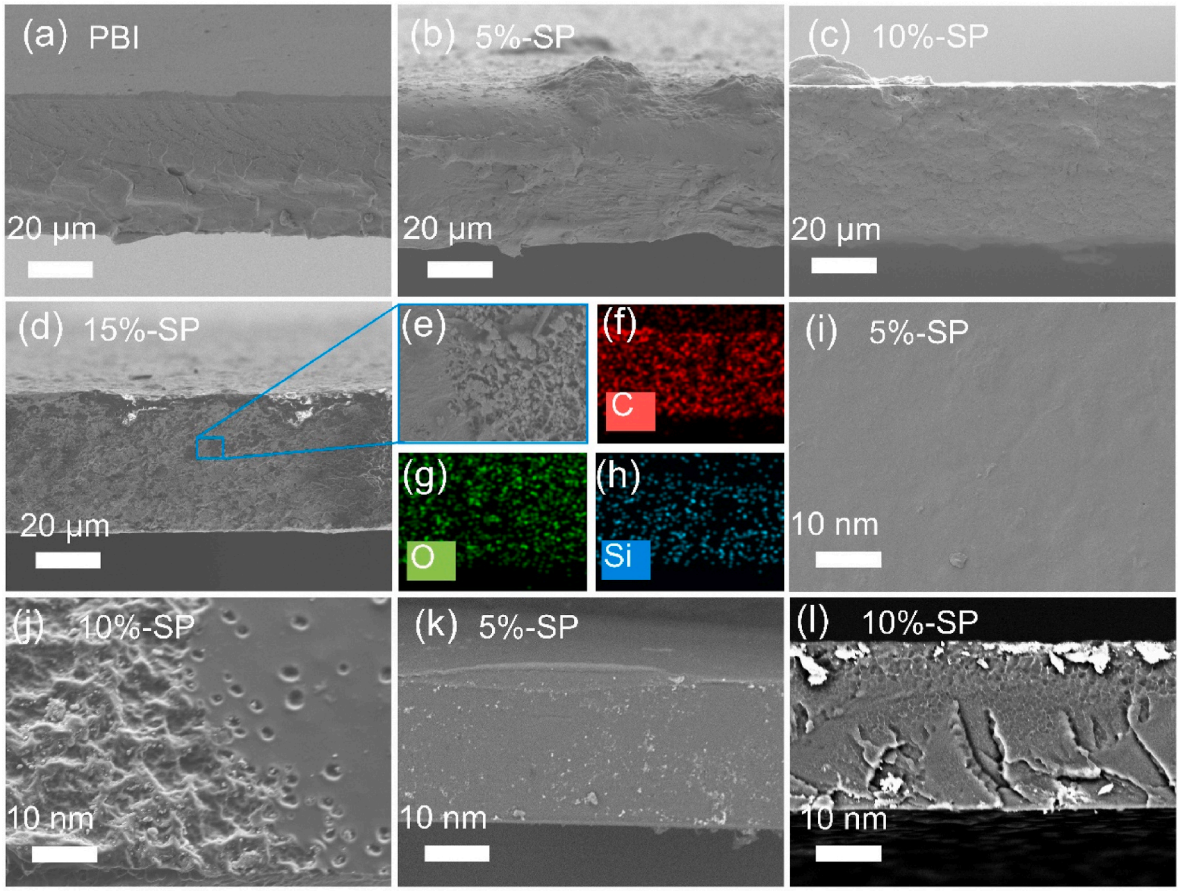

Fig. 5. The cross-section SEM images of (a) pristine PBI membrane, SiO_2/PBI composite membranes with the SiO_2 loadings of (b) 5 wt%, (c) 10 wt% and (d) 15 wt%. Image (e) is an enlarged image of the blue regions within the 15%-SP composite membrane. The elemental mappings of (f) carbon, (g) oxygen and (h) silicon elements in the 10%-SP composite membrane. The surface and cross-section SEM images of (i, k) 5%-SP and (g, h) 10%-SP composite membranes after heat-treatment at 220 °C for 48 h, where bright particles represent inorganic fillers within the PBI matrix. (For interpretation of the references to colour in this figure legend, the reader is referred to the Web version of this article.)

explore the *in situ* formed phosphosilicate on the stability of composite membranes, as shown in Fig. S1 and Table S1. After the heat-treatment at 220 °C for 48 h, the pristine PA/PBI membrane exhibits the high elongation of 86.9 % and tensile stress of 17.1 MPa. In contrast, the elongation of heat-treated 5%-SP and 15%-SP composite membranes decreased to 63.1 and 33.9 % and their tensile stress also declined to 13.8 and 11.3 MPa, respectively, indicating that the aggregation of $Si_5P_6O_{25}$ particles in PBI is responsible for the decreased mechanical strength of composite membranes. Fig. 1d exhibits the XRD pattern of the pristine PA/PBI and 5%-SP composite membrane after the heat-treatment at 220 °C for 48 h. Obviously, two broad peaks at around 19 and 27° are shown in both membranes, corresponding to P_2O_7 and P_2O_5 phases decomposed from PA at elevated temperatures [24]. Moreover, two small and broad peaks located at 23 and 25° in the 5%-SP composite membrane were detected, well matching with the $Si_5P_6O_{25}$ phase [24]. In comparison with the sharp and well-defined XRD patterns of $Si_5P_6O_{25}$ phase formed in the mixed SiO_2/PA samples after heat-treatment at identical 220 °C (see Fig. 1), the small and broad characteristic peaks associated with $Si_5P_6O_{25}$ phase indicate the existence of mixed crystalline and amorphous phosphosilicate phases *in situ* formed within SiO_2/PA/PBI composite membranes after heat-treatment at 220 °C. Thus, considering the balance between the microstructure and mechanical properties, the 5%-SP and 10%-SP composite membranes may offer the best potential for the conductivity and performance of HT-PEMFCs.

3.3. Conductivity and performance of the SiO_2/PA/PBI composite membranes

Fig. 6a shows the conductivities of SiO_2/PA gels with different SiO_2/PA ratios measured at 220 °C within 100 h. Obviously, their conductivities highly depend on the amount of introduced PA, i.e., the Si/P ratios. The initial conductivity was 194.3, 165.5 and 25.4 mS cm^{-1} for samples with Si/P molar ratios of 1/4, 1/1 and 1/1.2, respectively. The conductivity of SiO_2/PA samples decreases with the decrease in the PA content and their conductivity decrease rather rapidly in the early stage of measurements. For example, in the case of the sample with the highest Si/P molar ratio of 1/4, its conductivity dramatically dropped from 194.3 mS cm^{-1} to 74.7 mS cm^{-1} during the initial 12 h, reaching a stable value of around 60 mS cm^{-1} throughout the subsequent 100 h test. Although a portion of PA molecules were consumed during the $Si_5P_6O_{25}$ generation and thus led to a decrease in conductivity, the remaining PA could be adsorbed and bounded to the phosphosilicate phase, exhibiting a stable conductivity at the temperature higher than the boiling point of PA [39]. In addition, the conductivity of the as-prepared SP-48 sample varied between 42.5 and 97.4 mS cm^{-1} at the temperature range of 160 and 260 °C (Fig. 6b), while the conductivity of SP-48 after one washing (pH = 3.7) and after complete washing (pH = 6.8) decreased sharply and is 5 orders of magnitudes lower than that of as-prepared SP-48 sample (Fig. 6c). This indicates that the proton conductivity of pristine $Si_5P_6O_{25}$ phase is very low and negligible.

For the purpose of comparison, the pure $Si_5P_6O_{25}$ obtained from the completely washed SP-48 sample was re-mixed with PA and their conductivity was then measured at 220 °C. As shown in Fig. 6d, the mixture with the high $Si_5P_6O_{25}$/PA mass ratio of 1/2 has a high conductivity of 327.1 mS cm^{-1}, and decreased to 207.4 and 89.7 mS cm^{-1} for the samples with a lower $Si_5P_6O_{25}$/PA mass ratio of 1/1 and 2/1, respectively. However, all samples showed a downward trend throughout the stability test, especially in the initial 10 h. This is probably due to the rapid loss of PA content as the mixed $Si_5P_6O_{25}$/PA samples have a poor ability to retain PA in the mixture.

Fig. 7 shows the EIS spectra of pristine PA/PBI and SiO_2/PA/PBI composite membranes during the heat-treatment process. In the case of pristine PA/PBI membrane, its ohmic resistance (R_{ohm}) increased significantly from 0.14 Ω cm^2 at 160 °C to 0.39 Ω cm^2 at 250 °C, an increase of 0.25 Ω cm^2. The significantly increased membrane resistance is evidently due to the loss of PA at elevated temperatures. It has been reported that the acid leaching is promoted at high current densities or humidified conditions via the movement of water molecules, leading to the serious acid flooding in anodic GDLs and flow fields [11,13]. Interestingly, 5%-SP and 10%-SP SiO_2/PA/PBI composite membrane cells show a much stable cell resistance at elevated temperatures. For

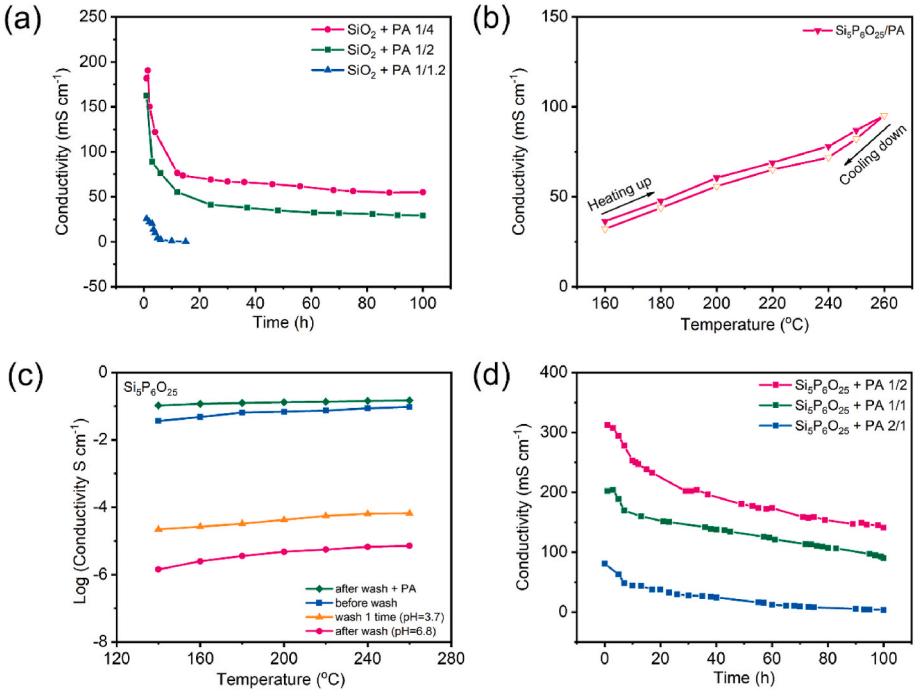

Fig. 6. The proton conductivity curves of (a) SiO_2/PA gels with the different Si/P molar ratio measured at 220 °C as function of time, (b) as-prepared SP-48 sample at the temperature range of 160–260 °C, (c) SP-48 sample before and after washing treatment and (d) proton conductivity stability of the $Si_5P_6O_{25}$/PA mixture with different mass ratios measured at 220 °C as a function of time, in which the pure $Si_5P_6O_{25}$ was prepared by completely washing the SP-48 sample.

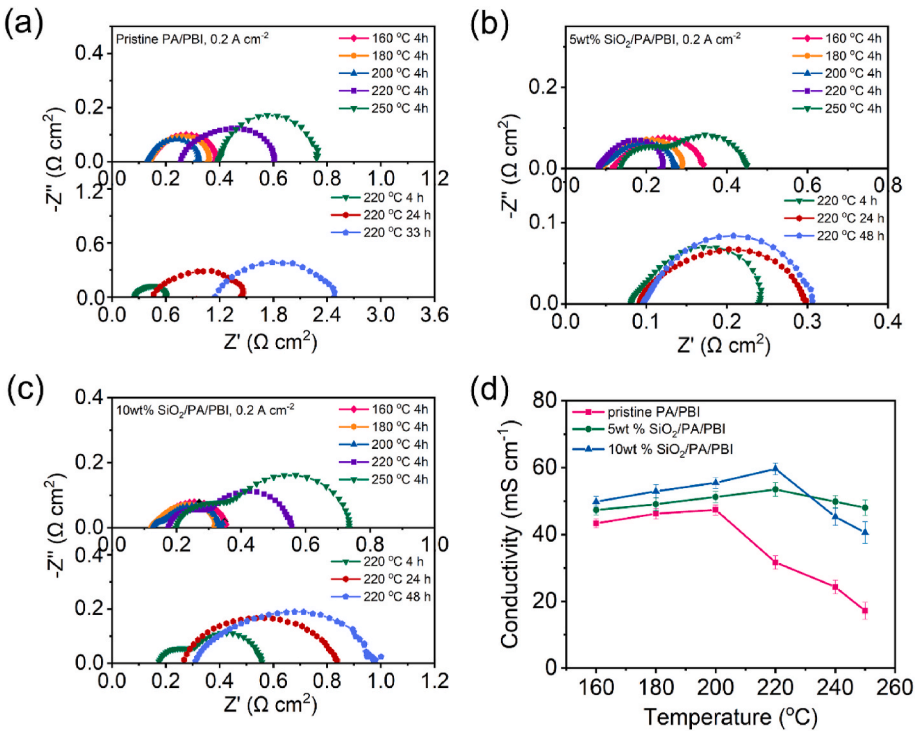

Fig. 7. EIS curves of (a) pristine PA/PBI, (b) 5%-SP and (c) 10%-SP composite membrane fuel cells, measured at the temperature range of 160–250 °C and a current density of 0.2 A cm^{-2}. All cells were kept at selected temperatures for 4h to stabilize the performance. (d) The proton conductivity of pristine PA/PBI, heat-treated 5%-SP and 10%-SP cells at the temperature range of 160–250 °C.

example, in the case of 5%-SP SiO_2/PA/PBI composite membrane cells, R_{ohm} changes from 0.11 Ω cm^2 at 160 °C to 0.14 Ω cm^2 at 250 °C, an increase of 0.03 Ωcm^2, much lower than that in the case of pristine PA/PBI membrane cell. This clearly indicates that the *in situ* introduced SiO_2 nanoparticles can effectively retain PA, thus alleviating the R_{ohm} increase for the composite membranes at elevated temperatures [17, 40]. Interestingly, 5%-SP and 10%-SP composite membrane single cells show two distinct semicircles at elevated temperature of 250 °C (see Fig. 7b and **c**). This is very different to the single overlapped arc observed for the reactions in HT-PEMFCs reaction at lower temperature range of 160–220 °C (see Fig. 7b and **c**). This is most likely due to the sluggish kinetic of the oxygen reduction reaction in cathode, which dominates the area specific resistance for HT-PEMFCs [41]. The appearance of two semicircles indicates the significantly enhanced kinetics of the ORR at elevated temperatures, in consistence with the reported significantly enhanced kinetics of the methanol oxidation reaction at elevated high temperatures [42].

The *in situ* formed predominantly amorphous phosphosilicate phase in PA/PBI membranes is beneficial to maintain the cell stability. After testing at 220 °C for 33h, the R_{ohm} and electrode polarization resistance, R_p for the pristine PA/PBI cell increased from 0.25 to 0.20 Ω cm^2 to 1.1 Ω cm^2 and 1.4 Ω cm^2, respectively. This is substantially higher than that observed on the 10%-SP composite membrane cell, which changes from 0.16 to 0.4 Ω cm^2 to 0.3 Ω cm^2 and 0.6 Ω cm^2, respectively, measured after testing at 220 °C for 48 h. Moreover, there is no noticeable increase in R_{ohm} for the 5%-SP composite membrane cell, while its R_p slightly increased from 0.15 Ω cm^2 to 0.21 Ω cm^2 after testing for 48 h. In Fig. 7d, the proton conductivity of pristine and composite cells is given as a function of the temperature. For the pristine PA/PBI membrane cell, a maximum conductivity of 47.4 mS cm^{-1} is achieved at 200 °C, followed by sharp decrease with increase in temperature and reaching 17.2 mS cm^{-1} at 250 °C. This is evidently caused by the acid evaporation and dehydration at elevated temperatures [13]. In comparison, introducing *in situ* formed predominantly amorphous phosphosilicate phase increases the conductivity of the composite membrane cells and in both cases, the maximum conductivity was observed at 220 °C, exhibiting 53.5 mS cm^{-1} for the 5%-SP membrane cell and 59.6 mS cm^{-1} for the 10%-SP membrane cell, respectively. Moreover, the *in situ* formed predominantly amorphous phosphosilicate is shown to alleviate the conductivity decreases, particularly in the case of 5%-SP composite membrane cell, achieving 48.1 mS cm^{-1} at 250 °C, much higher than 17.2 mS cm^{-1} measured on pristine PA/PBI membrane cell. This is attributed to the favorable acid retention ability of *in situ* formed hygroscopic and also predominantly amorphous phosphosilicate phase [24].

The distribution of relaxation times (DRT) was applied to analyze the measured EIS spectra of PA/PBI-based cells. Prior to the DRT fitting, all data were verified to have good reliability by the Kramers-Kronig relations (See Fig. S2) [43]. As shown in Fig. 8, several peaks located at high frequencies (above about 500 Hz) can be assigned to the hydrogen oxidation reaction (HOR) in the anode and proton transfer processes; the main peak between 10 and 500 Hz is attributed to the oxygen reduction reaction (ORR) in the cathode [44,45]. Typically, features related to the oxygen mass transfer should be distinguished below 10 Hz; however, no obvious peaks were shown in all EIS spectra as pure oxygen was introduced during the testing; namely, the oxygen transfer limitation affected by mass transfer process is negligible [44]. In pristine PA/PBI cells shown in Fig. 8a, the peak related to ORR process exhibits a growing tendency accompanied by the temperature increase, which is related to the variation or changes of three-phase boundaries in the cathode [24]. By contrast, all peak intensity of 5%-SP membrane cell decreased gradually when the operating temperature increased to 220 °C, suggesting that *in situ* formed phosphosilicate in membranes facilitates both of the proton transfer and ORR process. In the case of 10%-SP membrane cell, a series of increased peaks located at high frequency was observed at elevated temperatures (see Fig. 8c), revealing that the proton transport in anodic electrode was restricted. Although the immigrated PA driven by water molecules promotes the proton transfer and overall conductivity of HT-PEMFCs [46], excessive acid accumulation would reduce the H_2 partial pressure in anode, resulting in increased mass

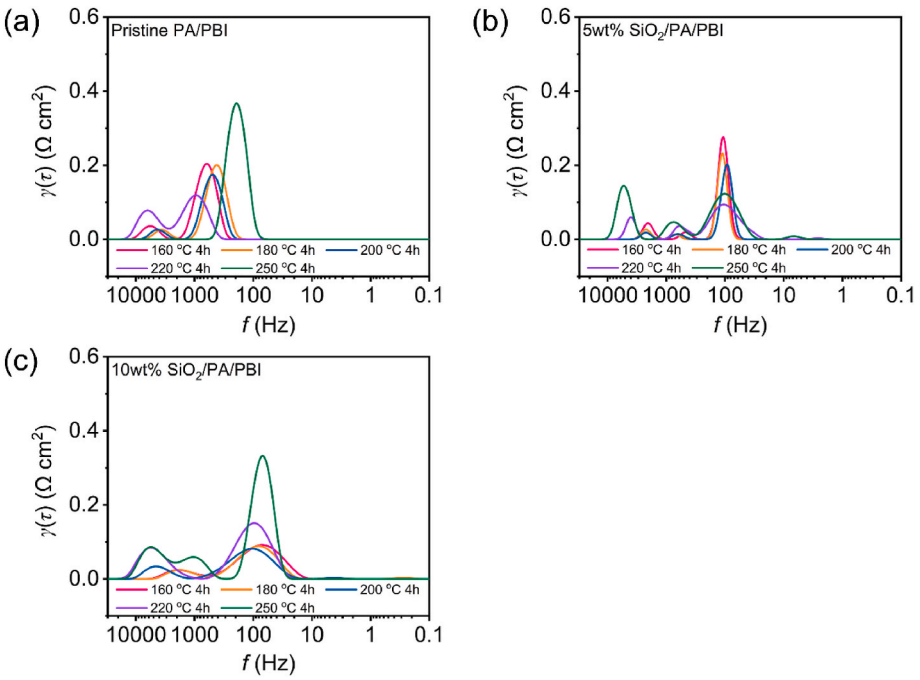

Fig. 8. Comparison of DRT plots at different operating temperatures for (a) pristine PA/PBI, (b) 5%-SP and (c) 10%-SP composite membrane cells.

transfer resistance and limited performance [47]. In addition, adjacent peaks at around 100 Hz slightly shifted toward lower frequencies, which could be explained by the enhanced ORR resistance at elevated temperatures [48].

Fig. 9 gives the polarization curves of pristine PA/PBI, 5%-SP and 10%-SP composite membrane single cells, measured at the temperature range of 160–250 °C with the constant H_2/O_2 flow of 150 mL min^{-1}. The peak power density (PPD) for pristine PA/PBI cell increased from 317.7 mW cm^{-2} at 160 °C to 407.3 mW cm^{-2} at 220 °C, while dropped catastrophically to 119.3 mW cm^{-2} at 250 °C. The sharp decrease in PPD of pristine PA/PBI membrane cell at elevated temperatures is consistent with its proton conductivity behavior as shown in Fig. 7a. The performance of the10%-SP composite membrane cell showed a similar tendency, which reached 457.2 mW cm^{-2} at 200 °C and declined to 226.2 mW cm^{-2} at 250 °C. By contrast, the 5%-SP composite membrane cell has a much better polarization behavior at elevated temperatures, showing a PPD of 530.6 mW cm^{-2} at 220 °C and 450 mW cm^{-2} at 250 °C (Fig. 9b). The power performance of 5%-SP composite membrane cell at 250 °C is substantially better than pristine and 10%-SP composite membrane cells, which is also superior than most HT-PEMFC performances based on composite membranes under identical test conditions (Table .1).

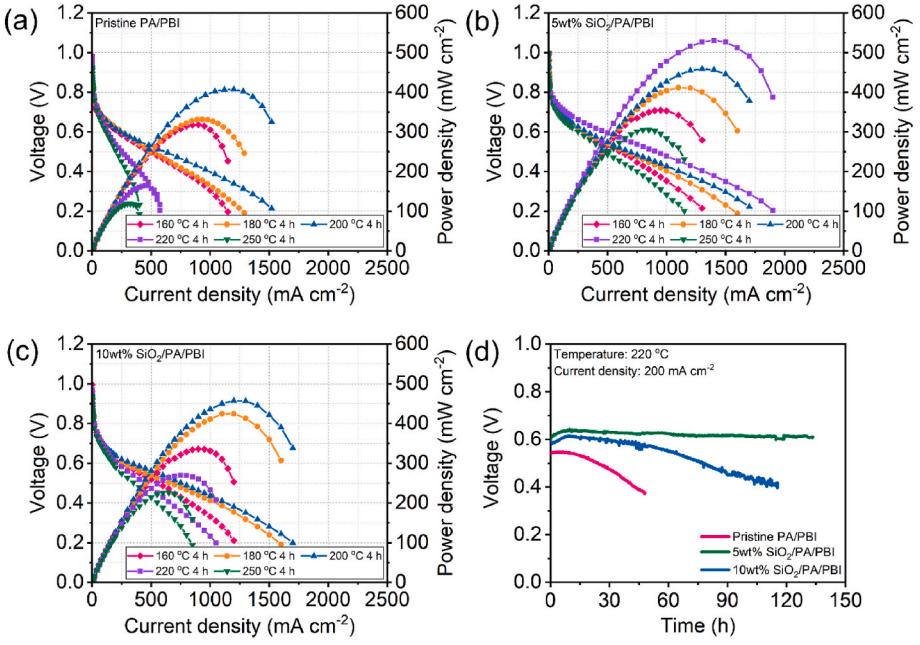

Fig. 9. Fuel cell polarization curves of (a) pristine PA/PBI, (b) 5%-SP and (c) 10%-SP composite membrane cells, measured at the temperature range of 160–250 °C. The composite membranes were pretreated at 220 °C for 48h. All cells were maintained at tested temperatures for 4 h with the constant H_2/O_2 of 150 mL min^{-1}. (d) The stability curves for pristine PA/PBI, 5%-SP and 10%-SP composite membrane cells, measured at 220 °C under a polarization current of 200 mA cm^{-2}.

Table 1
Fuel cell performance comparison of HT-PEMFCs based on composite membranes measured at elevated temperatures.

Inorganic fillers	Proton conductivity (mS cm^{-2})/T (°C)	Peak power density (mW cm^{-2})/T (°C)	Conditions	Ref.
$Sn_{0.95}Al_{0.05}P_2O_7$/PA/PBI	32/200	439.6/200	H_2/O_2	[49]
$Sn_{0.8}Sb_{0.2}P_2O_7$/PA/PBI	~40/210	670/175	H_2/Air	[50]
$CsH_5(PO_4)_2$/PA/PBI	~26/220	554/200	(H_2/Air, 20 % RH)	[51]
SnO_2/PA/PBI	30/280	264/220	H_2/Air	[52]
Nafion/SnP_2O_7-TBAP	~102/290	630/220	H_2/O_2	[36]
$Sn_{0.95}Al_{0.05}P_2O_7$/PA/PBI	40/250	840/200	H_2/O_2	[53]
PWA-*meso*-silica/PA/PBI	72/250	386/200	H_2/Air	[24]
$Ce_{0.9}Gd_{0.1}P_2O_7$/PA/PBI	199/180	125/250	H_2/O_2	[54]
SiO_2/PA/PBI	41/250	283/240	H_2/O_2	[25]
SnO_2/PA/PBI	51.3/250	476/250	H_2/O_2	[22]

Stability is the most important parameter of HT-PEMFCs at elevated temperatures. Fig. 9d exhibits the stability of assembled cells at 220 °C with a constant current of 200 mA cm^{-2}. The pristine PA/PBI membrane cell shows a fast degradation and the voltage drops from initial 0.54 V–0.37 V within 50 h, a degradation rate of 5.7 mV h^{-1}. The 10%-SP composite membrane cell shows a much better performance stability and the cell voltage decreases from initial 0.59 V–0.40 V within 120 h, a degradation rate of 1.6 mV h^{-1}. In contrast, a very stable performance was observed on the 5%-SP composite membrane cell. The initial cell voltage was 0.61 V and increased slightly to 0.63 V, essentially stable over 130 h at 220 °C and 200 mA cm^{-2}. To further understand the voltage loss of the 10%-SP membrane cell, the hydrogen crossover investigation was performed and results are shown in Fig. S3. Obviously, the 10%-SP composite membrane cell displayed a much higher H_2 crossover current density, indicating that aggregated $Si_5P_6O_{25}$ particles and inevitably formed structure defects in the composite membranes (see Fig. 6g) are responsible for the performance degradation. On the other hand, the hydrogen crossover current of 5%-SP membrane cell is very similar to the pristine PA/PBI membrane cell. This clearly shows that introducing 5 % SiO_2 in the composite SiO_2/PA/PBI composite membrane via the *in situ* formed predominantly amorphous phosphosilicate phase does not have detrimental effect on the microstructure of PA/PBI membranes, supported by the microstructure data (see Fig. 5).

This study clearly demonstrated that the *in situ* formed predominantly amorphous phosphosilicate phase in the SiO_2/PA/PBI composite membranes substantially enhanced the proton conductivity of the membrane, the cell performance and stability at elevated high temperature of 220 °C, and the best performance was obtained on SiO_2/PA/PBI composite membranes with 5 % SiO_2 addition. As shown in this study, *in situ* formed predominant amorphous phosphosilicate phase in 5%-SP composite membrane is uniformly distributed with no detrimental effect on the microstructure of the PBI polymeric matrix. Most important, the existence of predominant amorphous phase of phosphosilicates formed via the *in situ* generation process [40] effectively acts as an anchor for holding PA, alleviating the evaporation and leaching of PA and contributing to the excellent performance and stability of the composite membrane cells (see Fig. 9). However, excessive SiO_2 in the composite membrane leads to the agglomeration of formed phosphosilicates and thus affects its microstructure, mechanical strength, electrical conductivity and cell performance. This is evidently supported by the high power performance but relatively low stability of 10%-SP composite membrane cells.

4. Conclusion

In this work, the microstructure and conductivity properties of phosphosilicate phases derived from SiO_2 and PA precursors were investigated at different temperatures. The results indicate that the reaction of SiO_2 with PA occurs at 220 °C, forming well defined $Si_5P_6O_{25}$ crystalline phase. In comparison with the sharp and well-defined XRD patterns in the mixed SiO_2/PA samples after heat-treatment at identical 220 °C, the XRD patterns of the *in situ* formed SiO_2/PA/PBI composite membranes are characterized by the small and depressed peaks associated with $Si_5P_6O_{25}$ phase, indicating the existence of predominant amorphous phosphosilicate phases formed. Homogeneous SiO_2/PBI composite membranes can be prepared at the SiO_2 loading level of 10 wt %, however, *in situ* formed $Si_5P_6O_{25}$ particles trend to aggregate on membrane surfaces during the heat-treatment, which has negative impacts on not only mechanical strength of composite membranes but also the cell stability. The EIS and DRT analysis data illustrated that the distribution and aggregation of *in situ* formed amorphous phosphosilicate are responsible for the variation in performance and stability. The best results were obtained on the SiO_2/PA/PBI composite membranes with 5 wt% SiO_2 and with *in situ* formed amorphous phosphosilicate phases at 220 °C, exhibiting the high conductivity of 53.5 mS cm^{-1}, PPD of 530.6 mW cm^{-1}, and excellent stability at 220 °C for over 130 h. In conclusion, this study provides a simple but effective way to fabricate SiO_2/PA/PBI composite membranes with the *in situ* formed phosphosilicate phases for HT-PEMFCs to apply at elevated operating temperatures of 200 °C.

Declaration of competing interest

The authors declare that they have no known competing financial interests or personal relationships that could have appeared to influence the work reported in this paper.

Acknowledgment

This project was supported by the Australian Research Council under Discovery Project Scheme (DP180100731 and DP180100568).

Appendix A. Supplementary data

Supplementary data to this article can be found online at https://doi.org/10.1016/j.ijhydene.2024.01.095.

References

[1] Jeppesen C, Araya SS, Sahlin SL, Thomas S, Andreasen SJ, Kær SK. Fault detection and isolation of high temperature proton exchange membrane fuel cell stack under the influence of degradation. J Power Sources 2017;359:37–47.
[2] Andreasen SJ, Vang JR, Kær SK. High temperature PEM fuel cell performance characterisation with CO and CO_2 using electrochemical impedance spectroscopy. Int. J. Hydrog. Energy. 2011;36:9815–30.
[3] Zhang J, Xiang Y, Lu SF, Jiang SP. High temperature polymer electrolyte membrane fuel cells for integrated fuel cell - methanol reformer power systems: a critical review. Adv. Sustain. Syst. 2018;2:1700184.
[4] Aili D, Henkensmeier D, Martin S, Singh B, Hu Y, Jensen JO, et al. Polybenzimidazole-based high-temperature polymer electrolyte membrane fuel cells: new insights and recent progress. Electrochem Energy Rev 2020;3:793–845.
[5] Zhang J, Aili D, Lu SF, Li QF, Jiang SP. Advancement toward polymer electrolyte membrane fuel cells at elevated temperatures. Research 2020;2020:9089405.
[6] Araya SS, Zhou F, Liso V, Sahlin SL, Vang JR, Thomas S, et al. A comprehensive review of PBI-based high temperature PEM fuel cells. Int. J. Hydrog. Energy. 2016;41:21310–44.
[7] Aili D, Cleemann LN, Li QF, Jensen JO, Christensen E, Bjerrum NJ. Thermal curing of PBI membranes for high temperature PEM fuel cells. J Mater Chem 2012;22:5444–53.
[8] Yu S, Zhang H, Xiao L, Choe EW, Benicewicz BC. Synthesis of poly (2,2′-(1,4-phenylene) 5,5′-bibenzimidazole) (para-PBI) and phosphoric acid doped membrane for fuel cells. Fuel Cell 2009;9:318–24.
[9] Pingitore AT, Huang F, Qian G, Benicewicz BC. Durable high polymer content m/p-polybenzimidazole membranes for extended lifetime electrochemical devices. ACS Appl Energy Mater 2019;2:1720–6.

[10] Oono Y, Sounai A, Hori M. Long-term cell degradation mechanism in high-temperature proton exchange membrane fuel cells. J Power Sources 2012;210:366–73.
[11] Aili D, Becker H, Reimer U, Andreasen JW, Cleemann LN, Jensen JO, et al. Phosphoric acid dynamics in high temperature polymer electrolyte membranes. J Electrochem Soc 2020;167:134507.
[12] Bevilacqua N, George MG, Bazylak A, Zeis R. Phosphoric acid distribution patterns in high temperature PEM fuel cells. ECS Trans 2017;80:409–17.
[13] Søndergaard T, Cleemann LN, Becker H, Steenberg T, Hjuler HA, Seerup L, et al. Long-term durability of PBI-based HT-PEM fuel cells: effect of operating parameters. J Electrochem Soc 2018;165:F3053–62.
[14] Guo Z, Perez-Page M, Chen J, Ji Z, Holmes SM. Recent advances in phosphoric acid–based membranes for high–temperature proton exchange membrane fuel cells. J Energy Chem 2021;63:393–429.
[15] Kannan A, Aili D, Cleemann LN, Li QF, Jensen JO. Three-layered electrolyte membranes with acid reservoir for prolonged lifetime of high-temperature polymer electrolyte membrane fuel cells. Int. J. Hydrog. Energy. 2020;45:1008–17.
[16] Hu M, Li T, Neelakandan S, Wang L, Chen Y. Cross-linked polybenzimidazoles containing hyperbranched cross-linkers and quaternary ammoniums as high-temperature proton exchange membranes: enhanced stability and conductivity. J Membr Sci 2020;593:117435.
[17] Devrim Y, Devrim H, Eroglu I. Polybenzimidazole/SiO_2 hybrid membranes for high temperature proton exchange membrane fuel cells. Int. J. Hydrog. Energy. 2016;41:10044–52.
[18] Pinar FJ, Cañizares P, Rodrigo MA, Úbeda D, Lobato J. Long-term testing of a high-temperature proton exchange membrane fuel cell short stack operated with improved polybenzimidazole-based composite membranes. J Power Sources 2015;274:177–85.
[19] Ooi YX, Ya KZ, Maegawa K, Tan WK, Kawamura G, Muto H, et al. Incorporation of titanium pyrophosphate in polybenzimidazole membrane for medium temperature dry PEFC application. Solid State Ion 2020;344:115140.
[20] Li X, Ma H, Wang P, Liu Z, Peng J, Hu W, et al. Construction of high-performance, high-temperature proton exchange membranes through incorporating SiO2 nanoparticles into novel cross-linked polybenzimidazole networks. ACS Appl Mater Interfaces 2019;11:30735–46.
[21] Chiang Y-C, Tsai D-S, Liu Y-H, Chiang C-W. PEM fuel cells of poly(2,5-benzimidazole) ABPBI membrane electrolytes doped with phosphoric acid and metal phosphates. Mater Chem Phys 2018;216:485–90.
[22] Wang ZH, Zhang J, Lu SF, Xiang Y, Shao ZP, Jiang SP. Development of in situ formed metal pyrophosphates (MP_2O_7, where M = Sn, Ti, and Zr)/PA/PBI based composite membranes for fuel cells. Adv. Sustain. Syst. 2023;7:2200432.
[23] Özdemir Y, Üregen N, Devrim Y. Polybenzimidazole based nanocomposite membranes with enhanced proton conductivity for high temperature PEM fuel cells. Int. J. Hydrog. Energy. 2017;42:2648–67.
[24] Zhang J, Aili D, Bradley J, Kuang H, Pan C, De Marco R, et al. In situ formed phosphoric acid/phosphosilicate nanoclusters in the exceptional enhancement of durability of polybenzimidazole membrane fuel cells at elevated high temperatures. J Electrochem Soc 2017;164:F1615–25.
[25] Cheng Y, Zhang J, Lu S, Kuang H, Bradley J, De Marco R, et al. High CO tolerance of new SiO_2 doped phosphoric acid/polybenzimidazole polymer electrolyte membrane fuel cells at high temperatures of 200–250 °C. Int J Hydrog Energy 2018;43:22487–99.
[26] Poojary DM, Borade RB, Clearfield A. Structural characterization of silicon orthophosphate. Inorganica Chim Acta 1993;208:23–9.
[27] Matsuda A, Kanzaki T, Tadanaga K, Tatsumisago M, Minami T. Proton conductivities of sol–gel derived phosphosilicate gels in medium temperature range with low humidity. Solid State Ion 2002;154:687–92.
[28] Matsuda A, Kanzaki T, Tadanaga K, Tatsumisago M, Minami T. Medium temperature range characterization as a proton conductor for phosphosilicate dry gels containing large amounts of phosphorus. Electrochim Acta 2001;47:939–44.
[29] Massiot P, Centeno MA, Carrizosa I, Odriozola JA. Thermal evolution of sol–gel-obtained phosphosilicate solids (SiPO). J Non-Cryst Solids 2001;292:158–66.
[30] Tadanaga K, Michiwaki Y, Tezuka T, Hayashi A, Tatsumisago M. Structural change and proton conductivity of phosphosilicate gel–polyimide composite membrane for a fuel cell operated at 180 °C. J Membr Sci 2008;324:188–91.
[31] Tofield BC, Crane GR, Bridenbaugh PM, Sherwood RC. Novel phosphosilicate. Nature 1975;253:722–3.
[32] Nakamoto N, Matsuda A, Tadanaga K, Minami T, Tatsumisago M. Medium temperature operation of fuel cells using thermally stable proton-conducting composite sheets composed of phosphosilicate gel and polyimide. J Power Sources 2004;138:51–5.
[33] Xu X, Tao S, Wormald P, Irvine JTS. Intermediate temperature stable proton conductors based upon SnP_2O_7, including additional H_3PO_4. J Mater Chem 2010;20:7827–33.
[34] Poojary D, Borade R, Campbell III F, Clearfield A. Crystal structure of silicon pyrophosphate (form I) from powder diffraction data. J Solid State Chem 1994;112:106–12.
[35] Khabbouchi M, Hosni K, Mezni M, Srasra E. Structural characterizations and mechanical behavior of activated clay-based $Si_5(PO_4)_6O$ and SiP_2O_7 compounds. Silicon 2019;12:117–24.
[36] Ramaiyan KP, Herrera S, Workman MJ, Semelsberger TA, Atanasov V, Kerres J, et al. Role of phosphate source in improving the proton conductivity of tin pyrophosphate and its composite electrolytes. J Mater Chem A 2020;8:16345–54.
[37] Styskalik A, Skoda D, Moravec Z, Roupcova P, Barnes CE, Pinkas J. Non-aqueous template-assisted synthesis of mesoporous nanocrystalline silicon orthophosphate. RSC Adv 2015;5:73670–6.
[38] Guo Z, Chen J, Byun JJ, Perez–Page M, Ji Z, Zhao Z, et al. Insights into the performance and degradation of polybenzimidazole/muscovite composite membranes in high–temperature proton exchange membrane fuel cells. J Membr Sci 2022;641:119868.
[39] Lang S, Kazdal TJ, Kühl F, Hampe MJ. Diffusion coefficients and VLE data of aqueous phosphoric acid. J Chem Thermodyn 2014;68:75–81.
[40] Aili D, Zhang J, Dalsgaard Jakobsen MT, Zhu H, Yang T, Liu J, et al. Exceptional durability enhancement of PA/PBI based polymer electrolyte membrane fuel cells for high temperature operation at 200 °C. J Mater Chem A 2016;4:4019–24.
[41] Mack F, Laukenmann R, Galbiati S, Kerres JA, Zeis R. Electrochemical impedance spectroscopy as a diagnostic tool for high-temperature PEM fuel cells. ECS Trans 2015;69:1075–87.
[42] Cheng Y, Zhang J, Lu SF, Jiang SP. Significantly enhanced performance of direct methanol fuel cells at elevated temperatures. J Power Sources 2020;450:227620.
[43] Schönleber M, Klotz D, Ivers-Tiffée E. A Method for improving the robustness of linear Kramers-Kronig validity tests. Electrochim Acta 2014;131:20–7.
[44] Weiß A, Schindler S, Galbiati S, Danzer MA, Zeis R. Distribution of relaxation times analysis of high-Ttemperature PEM fuel cell impedance spectra. Electrochim Acta 2017;230:391–8.
[45] Zhang JJ, Wang HN, Li W, Zhang J, Lu D, Yan WR, et al. Effect of catalyst layer microstructures on performance and stability for high temperature polymer electrolyte membrane fuel cells. J Power Sources 2021;505:230059.
[46] Zhang C, Zhou W, Zhang L, Chan SH, Wang Y. An experimental study on anode water management in high temperature PEM fuel cell. Int J Hydrog Energy 2015;40:4666–72.
[47] Jalani NH, Ramani M, Ohlsson K, Buelte S, Pacifico G, Pollard R, et al. Performance analysis and impedance spectral signatures of high temperature PBI–phosphoric acid gel membrane fuel cells. J Power Sources 2006;160:1096–103.
[48] Bevilacqua N, Schmid MA, Zeis R. Understanding the role of the anode on the polarization losses in high-temperature polymer electrolyte membrane fuel cells using the distribution of relaxation times analysis. J Power Sources 2020;471:228469.
[49] Jin YC, Nishida M, Kanematsu W, Hibino T. An H_3PO_4-doped polybenzimidazole/$Sn_{0.95}Al_{0.05}P_2O_7$ composite membrane for high-temperature proton exchange membrane fuel cells. J Power Sources 2011;196:6042–7.
[50] Wu X, Mamlouk M, Scott K. A PBI-$Sb_{0.2}Sn_{0.8}P_2O_7$-H_3PO_4 composite membrane for intermediate temperature fuel cells. Fuel Clls 2011;11:620–5.
[51] Li Y, Hu J, Li H, Chen L. Performance of an intermediate-temperature fuel cell with a $CsH_5(PO_4)_2$-doped polybenzimidazole membrane. J Electrochem Soc 2022;169:024505.
[52] Wang X, Dong C, Zhao W, Gao P, Hou G, Chen S, et al. Core-shell tin pyrophosphate-based composite membrane for fuel cell with durability enhancement at elevated temperatures. Electrochim Acta 2024;475:143588.
[53] Lee K-S, Maurya S, Kim YS, Kreller CR, Wilson MS, Larsen D, et al. Intermediate temperature fuel cells via an ion-pair coordinated polymer electrolyte. Energy Environ Sci 2018;11:979–87.
[54] Singh B, Devi N, Srivastava AK, Singh RK, Song S-J, Krishnan NN, et al. High temperature polymer electrolyte membrane fuel cells with Polybenzimidazole-$Ce_{0.9}Gd_{0.1}P_2O_7$ and polybenzimidazole- $Ce_{0.9}Gd_{0.1}P_2O_7$-graphite oxide composite electrolytes. J Power Sources 2018;401:149–57.